

Article

Modeling of Integrated Nanoneedle-Microfluidic System for Single Cell Temperature Measurement

Salma Abdullah Binsilm, Maryam Alsadat Rad and Mohd Ridzuan Ahmad *

Department of Control and Mechatronics Engineering, Faculty of Electrical Engineering,
Universiti Teknologi Malaysia, Skudai, Johor 81310, Malaysia; sbinslem1@gmail.com (S.A.B.);
maryam.pd@utm.my (M.A.R.)

* Correspondence: ridzuan@fke.utm.my; Tel.: +60-7553-6333

Academic Editor: Fan-Gang Tseng

Received: 9 September 2016; Accepted: 28 October 2016; Published: 18 December 2016

Abstract: In this research, a finite element study on a nanoneedle-microfluidic system for single cell temperature measurement is presented. The nanoneedle design and electrical and mechanical characterization are analyzed, in which tungsten is used as the sensing material. A rectangular shaped sensor with a gap of 10.8 μm showed to give the same current density distribution within the nanoneedle, and a 90 nm^2 cross-sectional area showed to cause minimum damage to the cell. Furthermore, the current showed to have a positive temperature coefficient of resistance (TCR) with an increase in the temperature, and the nanoneedle showed to be able to resist ramp force up to 22.5 μN before failure. Electrical measurement on yeast cell showed that the nanoneedle was independent of the cell conductivity. The nanoneedle proved to be able to measure temperature with a current difference of 50 nA and a resolution of 0.02 $^{\circ}\text{C}$ in 10 ms. A Y-shaped microchannel was proposed and the microchannel cross-sectional area was optimized to be 63 μm^2 and a flow rate of 24.6 pL/min allowed successful cell penetration causing minimal damage to the cell.

Keywords: microfluidics; nanoneedle; intracellular temperature; finite element

1. Introduction

Single cell analysis has become an important field of research in which cell properties are studied for an improved understanding of cellular processes. Cell intracellular temperature has been proven a vital element in most cellular activities. Recently, many attempts by researchers focused on developing sensors that have high accuracy and do not cause any damages to the cells, such as nanogap biosensors [1], nanoneedle biosensors [2,3], and sensors using extended-gate field-effect transistors [4,5].

Micro total analysis system (μTAS) and lab on chip (LOC) attracted many researchers towards improving traditional detection techniques in many chemical, biological and medical areas. The added advantages that these systems provide, such as the ability to combine and automate all the analysis steps from sampling to obtaining data in a single chip, reduce total analysis time and are very cost effective encouraged the development of techniques that support many clinical applications including single cell analysis [6–8].

Single cell analysis is the type of study that considers the identity of individual cells and cell heterogeneity that made it an expanding field of research worldwide. Different cell properties include chemical, electrical, mechanical and thermal properties. The intracellular temperature of cells has shown to have important roles in cell functions, metabolisms, divisions and many other vital cellular activities [9–11]. In addition, cells that are characterized with an abnormality such as cancer tend to have higher heat production rates compared to normal cells [12].

Over the years, there have been many attempts to measure internal cellular temperature using different approaches [13]. Some relied on the luminescent change of materials to obtain the temperature gradient, e.g., quantum dots [14], nanoparticles [15], and thermosensitive materials [16,17]. These methods showed a high level of sensitivity. Yet, photo-bleaching, material movement inside the cell and toxicity are some critical disadvantages [18]. Other methods relied on material properties that were affected by temperature change. A nanoneedle based on thermocouple was one of the pioneer example that had an ability to detect 0.1 °C change in temperature [19]. A multi-walled carbon nanotube was suggested as a temperature detector for biological cells [20], as was photo acoustic microscopy (PAM), which measured the ultrasound signals induced by light absorption [21]. Another interesting idea was the incorporation of a microfluidic system with a resonant thermal sensor that measured heat generation in living cells, however, the application diversity was limited to a certain type of cells, i.e., brown fat cell (BFC) [22]. These non-luminescent sensors open the door for new fields of single cell thermal property studies which have the potential to produce highly sensitive measurements accurately.

In this study, a tungsten-based nanoneedle-microfluidic system is proposed for single cell temperature measurement. The nanoneedle design, characterizations, intracellular temperature detection and nanoneedle–microfluidic channel integration are studied. Considering the importance of finite element analysis as the initial step in designing a system, a thorough study was performed to optimize the necessary parameters that were believed to influence the final performance of the proposed system.

The nanoneedle design included a study on two parameters: the shape and size of the sensor, which had the best current density distribution and caused minimal damage on the *saccharomyces cerevisiae* cell under study. Then, the characterization analysis were on thermal-electric and mechanical characterizations to assess the ability of the nanoneedle to respond to temperature change as well as the nanoneedle's sustainability against external forces. Furthermore, the ability of nanoneedle to measure the temperature of a single cell was performed. Two factors were analyzed to effectively characterize the intracellular temperature of a single cell. The first factor was to test the effect of the cell conductivity on the nanoneedle performance, and the second was to evaluate the sensor sensitivity and response time to temperature change in the range of 24–60 °C. Lastly, the integration of the nanoneedle to a microfluidic channel required a study on the cell flow rate which was influenced by the microfluidic channel cross-sectional area and the fluid velocity.

2. Proposed Nanoneedle-Microfluidic System

2.1. System Concept and Design

The idea of the device is to integrate a thermal nano-sensor with a microfluidic channel to have a high throughput system for rapid analysis. The system design is shown in Figure 1a. The concept can be summarized as follows: By manipulating the flow rate of water using an external syringe pump through the inlet hole, cells will flow towards the nanoneedle and would have the necessary force imposed on it that will enable the penetration into the nanoneedle for temperature measurement, as shown in Figure 1b,c.

The detection is done by applying voltage to the electrodes of the nanoneedle and measuring the output current for results. The current value will change corresponding to the change in the internal temperature of the cell. The nanoneedle works in the same principle as the resistance temperature detectors (RTD) having a positive temperature coefficient of resistance (TCR). The sensing element was chosen to be of tungsten for its high electrical conductivity, mechanical strength and promising fabrication procedure [23–25]. The rigidity of Tungsten and the small size of the nanoneedle ensure higher chances of penetration. Equations (1) and (2) [26] present the working principle of the sensor.

$$V = R \times I \quad (1)$$

$$\rho = -1.06871 + (2.06884 \times 10^{-2} \times T) + (1.2797110^{-6} \times T^2) + (8.5310110^{-9} \times T^3) - (5.1419510^{-12} \times T^4) \quad (2)$$

V is the voltage (V), I is the current (A), R is the resistance (Ohm), (ρ) is related the resistivity which relates resistance to temperature, and T is the temperature (K).

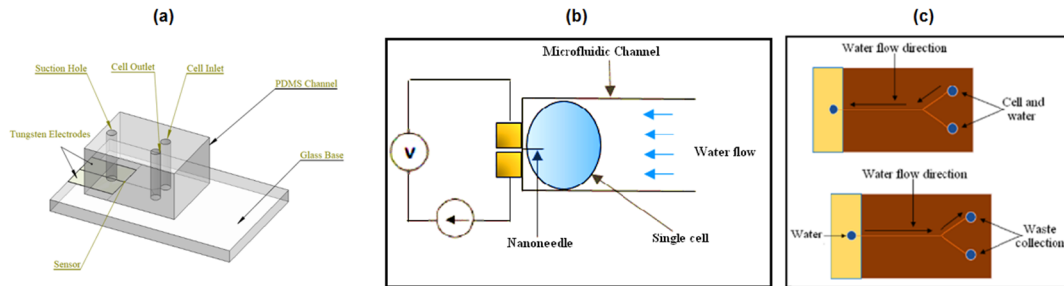


Figure 1. (a) Proposed microfluidic system design, the system concept and working principle; (b) Schematic diagram illustrating how cells penetrate the nanoneedle for measurement; (c **top**) The microfluidic channel when cells are inserted into the chip for measurement; (c **bottom**) The location and direction of water after the measurement and for waste collection.

2.2. Simulation Analysis Setup

In this work, the simulation analysis was done using ABAQUS (Version: 6.12, Dassault Systemes, Vélizy-Villacoublay Cedex, France) finite element analysis software that performs multi-physics analysis. Different settings were implemented for each stage in the modeling process depending on the parameters and condition under study. For instance, in the designing (shape, gap and size) and electrical and mechanical characterization of the nanoneedle, the objectives of the simulation are to have an equally distributed current density within the nanoneedle, to obtain the nanoneedle that causes minimal damage to the cell under study. This is performed to have the same behavior as a positive RTD, and to have high strength to be able to penetrate the cell/cell wall. This involved the use of electrical-thermal and mechanical definition. The nanoneedle was modelled as a 3D solid deformable DC3D4E with a 4-node linear coupled thermal-electrical element for the nanoneedle shape and size optimization. The nanoneedle shape of either being square or a circular (Figure 2) and the gap length within the nanoneedle were studied (Figure 2b), the uniformity of current density distribution was the determining factor. The cross-sectional area size of the nanoneedle was analyzed based on the damage the nanoneedle caused a yeast cell after penetration (Figure 3a). The nanoneedle position on a 4 μm yeast cell model is shown in Figure 3b. The yeast cell was modelled as a solid deformable C3D8R with an 8-node linear brick 3D stress element for mechanical model. The cell model had two main components: the cell wall and cytoplasm. The size was varied between 4 and 6 μm in diameter depending on the purpose of the simulation. Here a 4 μm yeast cell was used. The cell wall was defined as a hyper-elastic material with properties defined from [22] and the cytoplasm as homogenous fluid.

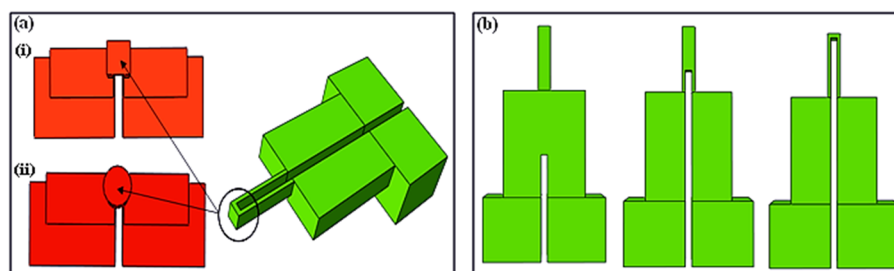


Figure 2. The nanoneedle design highlighting the shape and the gap to be studied. (a,i) Square (a,ii) Circular; (b) Gap length performed in the nanoneedle design optimization.

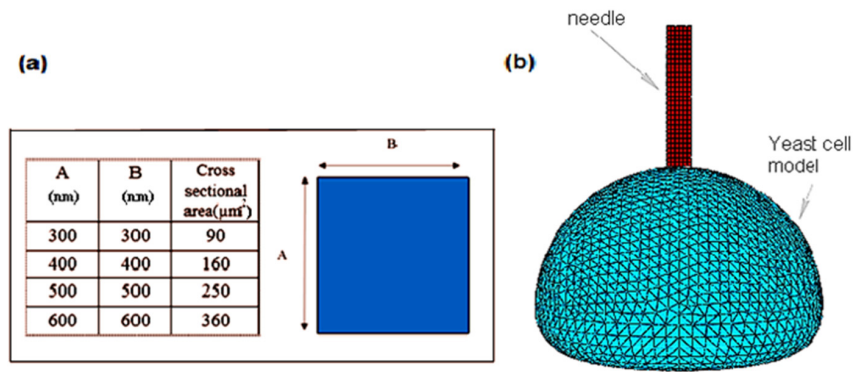


Figure 3. (a) Cross-sectional area to be studied; (b) The nanoneedle position on a 4 μm yeast cell model.

The second stage in the modelling was to characterize the nanoneedle behavior prior to the integration. Firstly, it was the electrical characterization, which a deformable DC3D4E model was used to model the nanoneedle for the thermal-electric characterization with a 4-node linear coupled thermal-electric element definition. Density, specific heat, electrical and thermal conductivity of tungsten were defined and a 0.1 hexahedron meshing size was applied. The aim of this simulation was to observe the behavior of the current within the nanoneedle and if it complies with the behavior of a positive RTD. A constant voltage of 1 volts was applied at one surface of the electrodes and ground to the other (Figure 4a). The current density change was observed as the temperature varied. The temperature was defined at the surrounding in the pre-defined field as a preliminary step for the temperature to stabilize and have an even distribution within the needle prior to the application of the voltage.

Secondly in the mechanical characterization, the nanoneedle was modeled as a 3D solid deformable C3D8R with an 8-node linear brick 3D stress element. Density, elastic, plastic and failure properties were defined for tungsten and a 0.1 hexahedron meshing size was applied. Ramp force was applied to the top surface of the needle where the penetration happens, and fixed at the bottom surface of the electrodes where it would attach to the glass plate in the microfluidic system (Figure 4b). The mechanical characterization was performed to examine the nanoneedle behavior when exposed to external forces. The displacement of the nanoneedle was obtained to identify the bending it will undergo before failure when forces are applied. The damage and strain energy outputs were studied to obtain the maximum force the nanoneedle could withstand before breakage.

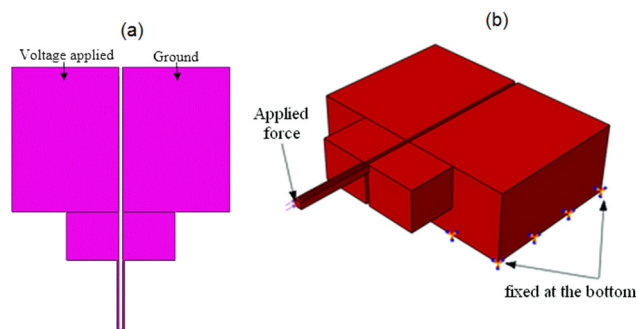


Figure 4. (a) Thermal/electric characterization simulation setup; (b) Simulation setup of the nanoneedle mechanical.

The third stage in the modelling was to study the performance of the nanoneedle and its response after penetrating a cell. Two steps were done to assess the performance correctly: electrical measurement on the cell, and the response to temperature change to obtain temperature versus current. The electrical measurement was done to determine the effect of the cell conductivity on

the nanoneedle. According to the literature, single cell viability could be detected by measuring the current flow inside a cell using dual nanoprobes made of tungsten [2]. This triggered the possibility that the cell conductivity could affect the temperature measurement. Therefore, the dependency of the nanoneedle conductivity on cell conductivity had to be clearly attained. In the simulation setup, two main components were used: the nanoneedle and yeast cell model. The simulation setup proposed was mimicking the situation that would happen after the penetration (Figure 5a). The nanoneedle was assembled and merged with the cell model into one part defined using a 4-node linear coupled thermal-electric element definition. A constant voltage value of 1 volts was applied at one surface of the electrodes and ground to the other, as shown in Figure 5b. The simulation was defined at room temperature and the output current density was obtained and compared to the value from the nanoneedle characterization.

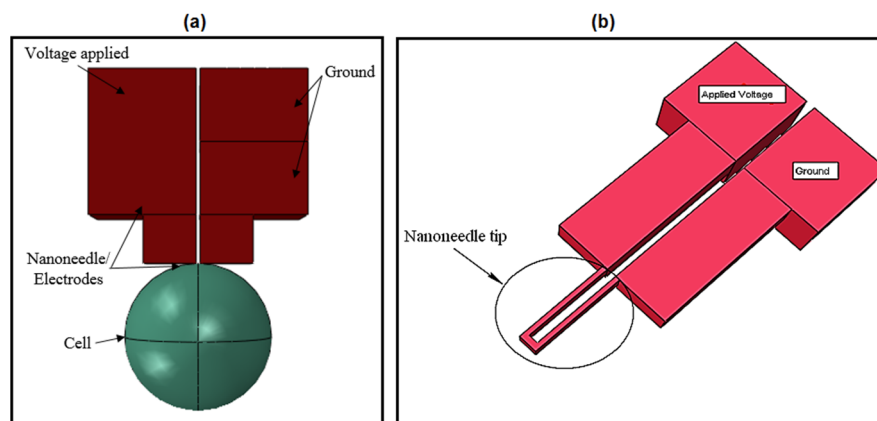


Figure 5. (a) Simulation for the single cell electrical measurement; (b) Schematic diagram of the nanoneedle showing the nanoneedle tip.

The fourth stage of developing the nanoneedle-microfluidic system was to design the microfluidic channel and analyze the water behavior in the channel. The microfluidic system was designed to have two major components, the Polydimethylsiloxane (PDMS) channel and an external pump to control the fluid flow rate. These components were studied and constructed in a way to achieve single cell penetration and thermal characterization.

Fluid flow rate inside the microfluidic channel was designed to play a crucial role in the proposed nanoneedle-microfluidic system. It is responsible to push the cells towards the nanoneedle and create the required force for successful penetration. The integrated nanoneedle-microfluidic system required microchannel height optimization and velocity optimization to have the range at which successful penetration could be achieved. The microfluidic channel required height optimization due to the disturbance in the water flow caused by the nanoneedle electrodes after the integration. Water flowed in the opposite direction and backward velocity was observed that disturbed the water distribution throughout the microchannel and the penetration process. This happened to be causing cell damage as well (Figure 6). Thus, the channel height had to be optimized at first with the aims of achieving full cell penetration, minimum cell damage, and least backward velocity. The channel width was maintained at 7 μm in order to minimize the number of cells entering the channel.

The analysis was done using a 6 μm yeast cell, nanoneedle, microchannel (Figure 7a) and water. The water was defined as a eulerian EC3DR model with a 4-node linear eulerian brick element definition. Density, equation of state, and viscosity of water were defined and 0.2 hexahedron meshing size was used. The parameter under study was the microchannel height by varying its value between 7 to 9 μm (Figure 7b) and maintaining the velocity constant at 6.5 $\mu\text{m}/\text{s}$. The velocity was defined on water in the predefined field and remained flowing throughout the simulation until the penetration occurred.

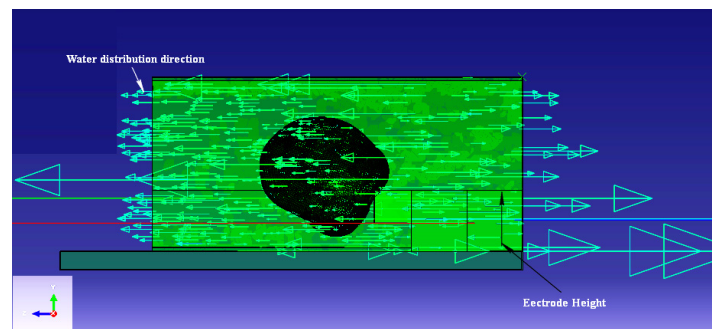


Figure 6. Backward velocity resulting from the electrode height.

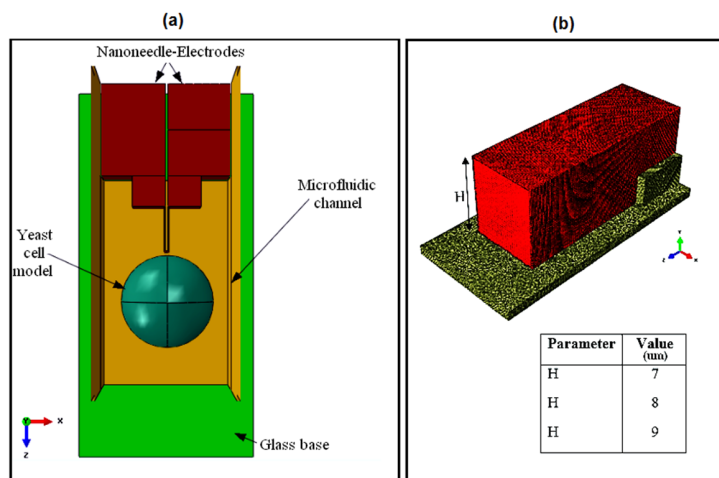


Figure 7. (a) Flow rate optimization simulation setup; (b) Height manipulation for simulation of flow rate optimization.

After optimizing the channel height, the velocity range at which successful penetration could be achieved had to be determined in order to optimize the flow rate range to be used by the external micropump for the nanoneedle/microfluidic system. The simulation setup of the velocity analysis was the same as the height optimization simulation setup described, however, instead of maintaining the velocity constant, the optimized cross-sectional area was kept constant and the velocity was manipulated. The velocity values were varied between 5, 5.5, 6, 6.5 and 7 $\mu\text{m/s}$, and the cell penetration depth was the key determining factor for the optimized velocity value and thus optimize the water flow rate. The penetration depth was considered successful when the nanoneedle was fully penetrated without excessive penetration, which could be viewed by changing the cell shape.

In the final stage, the cell flow direction in the channel at different time was analyzed. Three *S. cerevisiae* cells were modeled using yeast cell mechanical properties definitions with a mesh size of 0.1. The optimized velocity of 6.5 $\mu\text{m/s}$ was applied at the inlet, and the other ends were set to open, which indicates that there is no resistance to water flowing towards it.

3. Results and Discussion

The analysis covered the design, characterizations, intracellular temperature detection and nanoneedle-microfluidic channel integration. Figure 8 illustrates the simulation results of the first stage of the designing process, covering mainly the nanoneedle design. The gap was the first factor considered in the analysis, as it is evident in Figure 8a,b.

The current density shown by the color bar did not flow to the tip of nanoneedle (where the detection would happen after penetration) when the gap was only at the electrodes. As the gap increased towards the tip, the current density distribution was more noticeable within the nanoneedle.

However, the current density did not achieve uniformity, which would affect the accuracy of the measurement. This was solved by manipulating the cross-sectional area shape from being circular to a square (Figure 8c,d). The final selected design (Figure 8e) had an even current density distribution throughout the sensor, a gap of 10.8 μm and a square cross-sectional area.

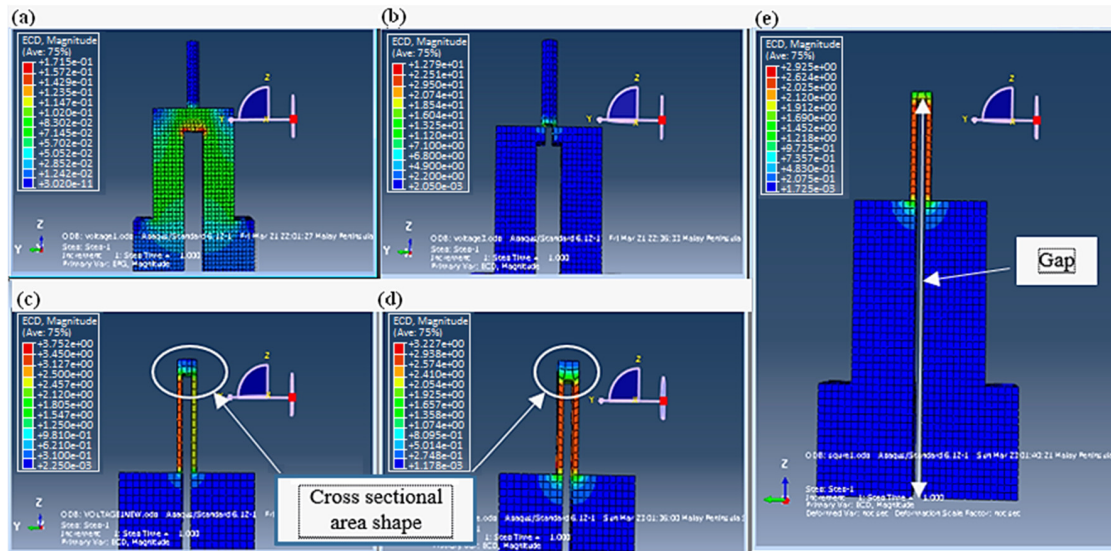


Figure 8. Diagram showing the results of the nanoneedle design highlighting the shape and the gap studied. (a,b) The current distribution with the sensor due to the gap effect manipulation; (c,d) The cross-sectional shape effect on the current distribution; (e) The current density distribution due to a gap of 10.8 μm and a square cross-sectional area.

After the cross-sectional area shape was decided, the size was analyzed by viewing the effect of the penetration of different nanoneedle sizes (90, 160, 250, 360, 490 nm²) into a yeast cell (Figure 9a–e). As can be seen, all the nanoneedle sizes could penetrate the cell with the same applied force without causing any immediate bursting. However, the damage (scale of 0 in blue color and 1 in red color) of the inner part of the cell wall (marked in red circles) increased as the cross-sectional area of the nanoneedle increased. This can be explained by the increased pressure on the cell when a larger surface is pressing against it. From the Figure 9a, the damage caused by the 90 nm² cross-sectional area was the most reasonable as it did not cause any tearing of the inner cell wall. Thus, the final design was chosen with a gap of 10.8 μm and a 90 nm² square shaped cross-sectional area.

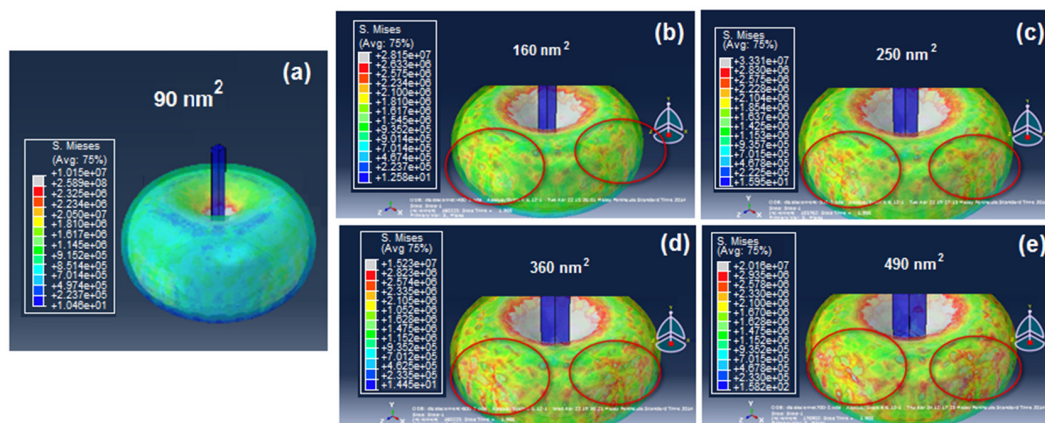


Figure 9. The penetration effect of the different nanoneedle sizes (cross-sectional areas) of (a) 90 nm²; (b) 160 nm²; (c) 250 nm²; (d) 360 nm²; and (e) 490 nm² on the single cell. The red circles shows the damage of the inner part of the cell wall.

The second stage of the designing was the characterization of the nanoneedle. Thermal/electric characterization was performed in order to characterize the nanoneedle response to temperature and validate whether it follows the concept of the resistance temperature detectors that the design was based on. Figure 10a,b present the simulation results of the current density of the nanoneedle defined at 293.15 K (room temperature) and 333.15 K. It was observed from the results that the intensity of current density decreased as the temperature increased. The behavior was the same as the resistance temperature detector's (RTD) response to temperature, which confirms the concept.

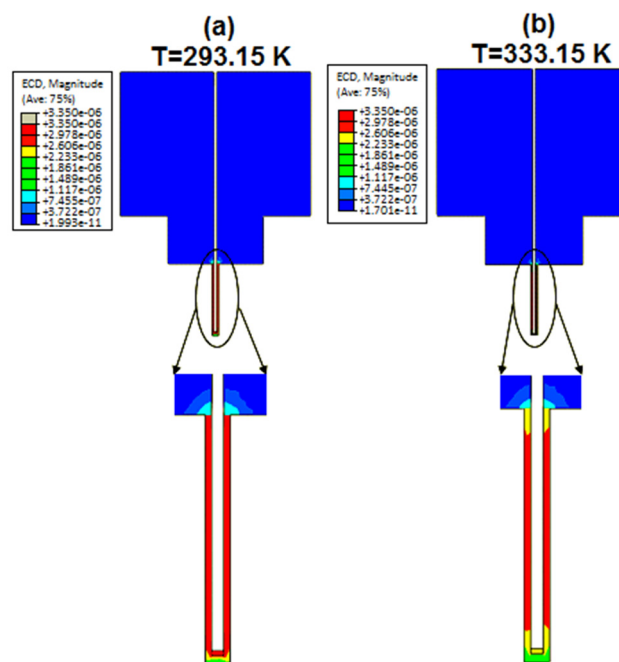


Figure 10. Simulation results of the thermal electric characterization. (a) Current density at 293.15 K and (b) 333.15 K.

Mechanical characterization of the nanoneedle was done to characterize the needle performance under the effect of external forces. When an external force was applied, pressure was clearly observed at the nanoneedle tip, which indicated the location prone to damage (Figure 11a). Furthermore, displacement of the nanoneedle tip study was done to determine the effects of the forces applied on the nanoneedle, which will cause it to start to bend (Figure 11b). The graph showed that as the forces gradually increased, the displacement increased, and would overshoot when the force approximately reached 12 μN . This could be explained that the nanoneedle started to undergo permanent deformation and the bonds between the molecules weakened, which will need to be calibrated to perform successful measurements.

Figure 12a shows the results of the nanoneedle damage. The maximum force that can be applied to the nanoneedle was 22.5 μN . This is sufficient for the purpose of cell penetration in particular yeast cell, as it has been proven that a force of up to 1 μN was needed for yeast cell penetration [23]. The plot of the strain energy versus the force applied in Figure 12b further confirmed the force at which the damage occurred since the strain drastically dropped when the force reached 22.5 μN .

The third stage was the electrical measurement on *S. cerevisiae* cell. Figure 13a,b show the simulation results of the voltage and the current density obtained from the *S. cerevisiae* cell electrical measurement.

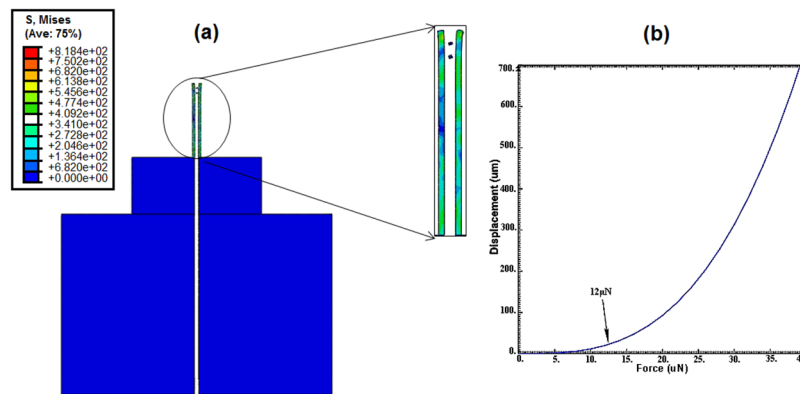


Figure 11. Simulation result showing the pressure on the nanoneedle because of applying external forces. (a) The graph shows the location that had the effect under pressure; (b) Displacement of the nanoneedle as the force increased, the graph overshoot at 12 μN .

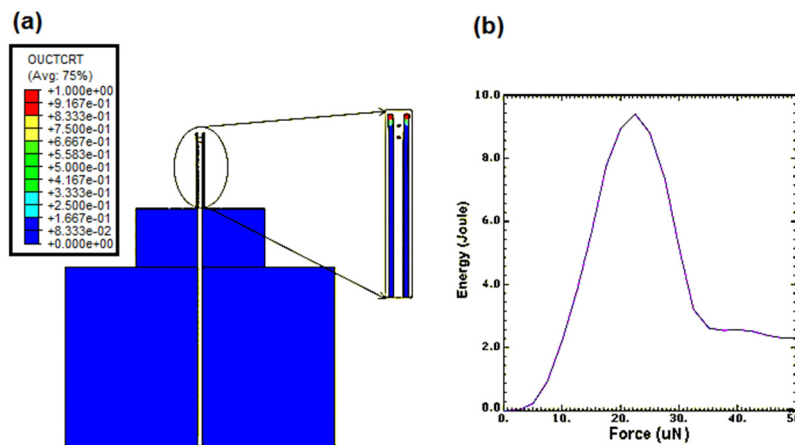


Figure 12. Simulation results of the mechanical characterization, which shows the damage on the nanoneedle. (a) The failure caused by the external forces when exceeding 22.5 μN ; (b) The strain energy of the nanoneedle; it drastically dropped when the force exceeded 22.5 μN .

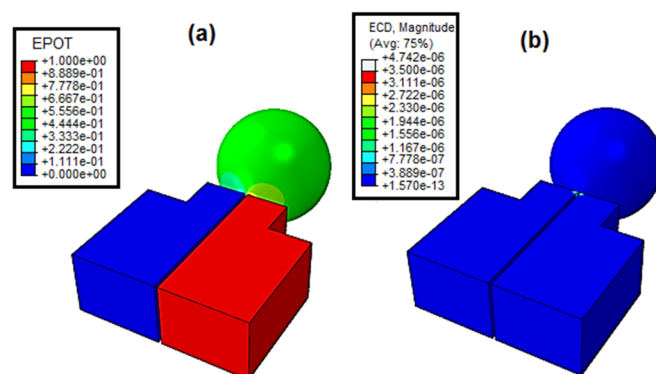


Figure 13. Simulation results of the single cell electrical measurement. (a) The voltage drop across the cell results; (b) The current density results.

As shown, the voltage clearly passed through the cell, which means that the voltage drop direction passed through the cell, confirming that the current had a path through the cell. From the current density shown in Figure 13b, the current density value was not different than the value obtained in Figure 10, which was done independent of the cell. This confirms that the cell conductivity had no

effect on the nanoneedle conductivity. This also could be validated by comparing it to the current measurement of yeast cell obtained in [23] that was only in 262 pA. To further understand the analysis, a cross-sectional view was taken and presented in Figure 14a,b. From the results, the color legend clearly showed that the current passed through the nanoneedle and was absolutely independent of the cell conductivity. In addition, the direction the current took to reach the ground shown in Figure 14b was only within the nanoneedle. This further confirms that the measurement of the temperature is independent of the cell and it is only dependent on the nanoneedle conductivity characteristic and its intrinsic properties that change with the temperature.

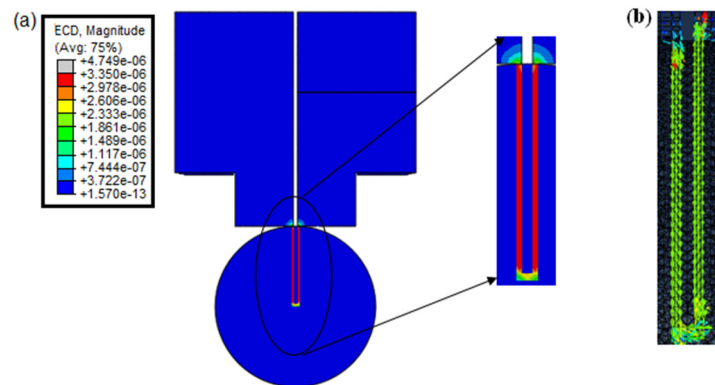


Figure 14. (a) Cross-sectional view of the current density results; (b) Zoomed image of the direction of the current flow. This confirms that the temperature measurement is independent of the cell conductivity.

The second analysis was done to determine the temperature detection abilities of the nanoneedle. A plot of the current change as a function of temperature ranging from 293.15–333.15 K is shown in Figure 15. The behavior of the graph showed the same behavior as an RTD with a positive TCR: a decrease in the current as the temperature increased, which has an inverse relation to the resistance. The results confirmed that the nanoneedle was able to detect the temperature in the required range with a sensitivity of 0.015 °C having a difference of approximately 50 nA between the minimum and the maximum temperature. Another study was to examine how fast the nanoneedle responded to temperature change in the surrounding. The temperature difference was set to be 0.02 °C by setting the surrounding temperature to 293.17 K and the temperature of the nanoneedle at 293.15 K. Figure 16a illustrates the transition the nanoneedle undertook while attempting to come in equilibrium with the surrounding temperature. Figure 16b shows the temperature response after it came into equilibrium with the surrounding temperature; the plot showed that the nanoneedle took 10 ms to come in equilibrium with the surrounding temperature. The results presented show that the nanoneedle can react to temperature in a very fast time with high sensitivity, which is very important in single cell temperature measurements.

The fourth stage of the analysis was to optimize the microchannel height and the velocity for successful penetration. Figure 17 shows the simulation results of the microchannel height optimization analysis. The channel height had a strong effect on the cell flow and penetration into the nanoneedle. The higher the height, the better the flow was and the more penetration was observed on the cell. This could be explained by the effect of the water flow distribution that was disturbed by the electrode structure in the microchannel (Figure 18). By comparing the backward velocities in channel heights of 7, 8 and 9 μm , the velocity flow in the opposite direction of the nanoneedle was higher as the channel height decreased (indicated by the red arrow and the highest legend value in Figure 18). Furthermore, there was a noticeable forward velocity flowing towards the nanoneedle in the all heights. However, the 8 μm channel height had more forward flow distribution towards the nanoneedle compared to the 7 μm but with clear backward velocity. The 9 μm channel height, had no obvious backwards velocity and more forward velocity flow in the channel.

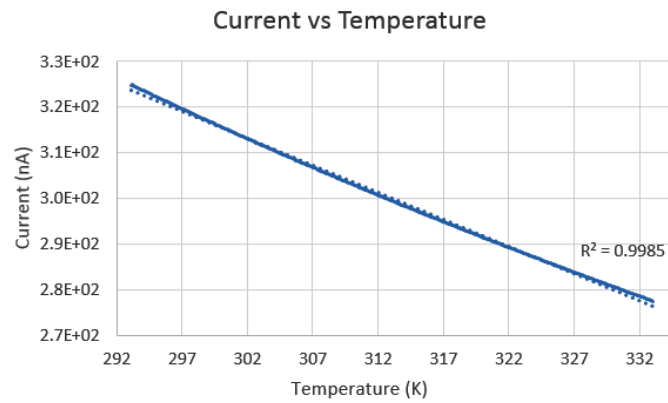


Figure 15. Current change in the nanoneedle with the temperature.

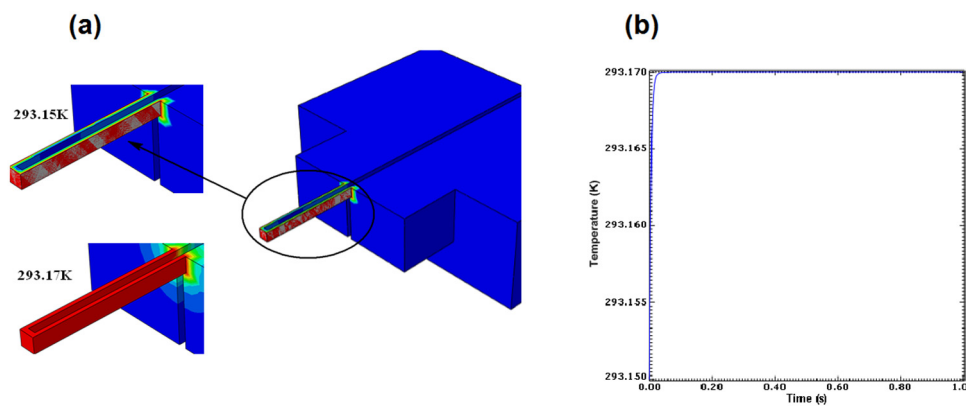


Figure 16. (a) Graph shows the nanoneedle transition with temperature change of 0.015 °C; (b) Plot of the time the nanoneedle took to adapt to the surrounding temperature.

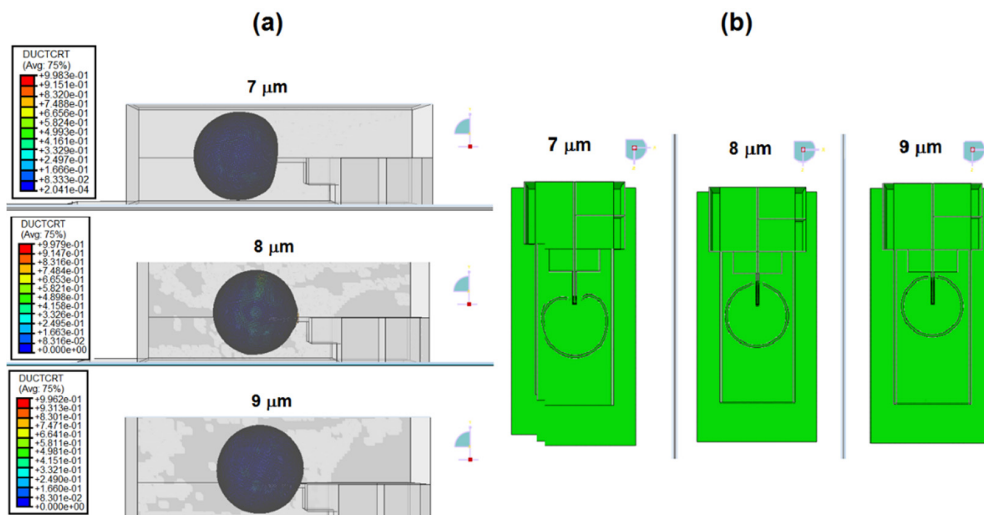


Figure 17. (a) The side view and (b) top view of the penetration depth of the cell into the nanoneedle in 7, 8, and 9 μm channel heights.

After optimizing the channel height, the velocity range at which successful penetration could be achieved had to be determined in order to optimize the flow rate range to be used by the external micropump for the nanoneedle-microfluidic system. Figure 19 presents the simulation results for flow rate optimization. Figure 19a displays the side view of the penetration, while Figure 19b shows the top view of the penetration depth. At first, the velocity was set to 5 μm/s, which was equivalent to

18.9 pL/min and was gradually increased to 7 $\mu\text{m/s}$ to study the penetration behavior. From the results, velocities 5 and 5.5 $\mu\text{m/s}$ did not show any signs of penetration, in fact, velocity 5.5 $\mu\text{m/s}$ overtook the nanoneedle and flew towards the upper part of the microchannel. Velocity 6 $\mu\text{m/s}$ showed some penetration; however, it was insufficient as the cell penetrated to the center of the nanoneedle and stopped due to the backward velocity pushing the cell, when the aim was to penetrate and to fully cover the nanoneedle. The most suitable velocity was 6.5 $\mu\text{m/s}$, which displayed successful penetration. Lastly, velocity 7 $\mu\text{m/s}$ caused excessive penetration and the cell was squashed into the nanoneedle electrodes, which caused the shape to slightly deform. Consequently, the optimum velocity range for cell penetration would be between 6.5 to 6.9 $\mu\text{m/s}$. Below that range, the cell will not penetrate to the desired location, and above that range, the cell will over-penetrate and may lead to cell damaged. Table 1 summarizes the results of flow rate optimization.

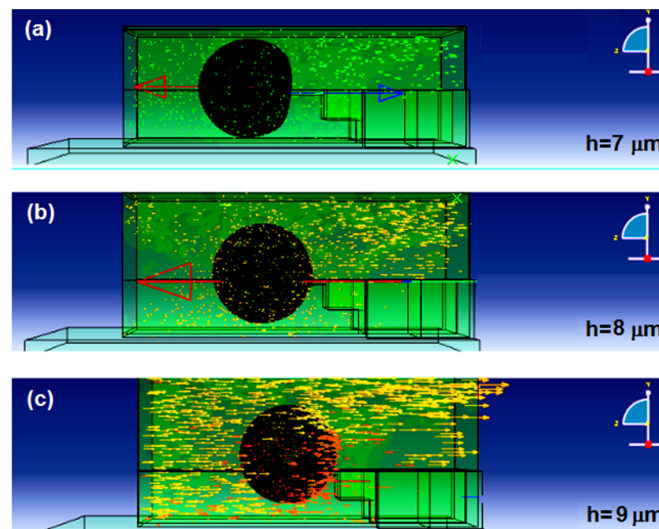


Figure 18. Velocity distribution within the (a) 7 μm ; (b) 8 μm ; and (c) 9 μm channel heights h .

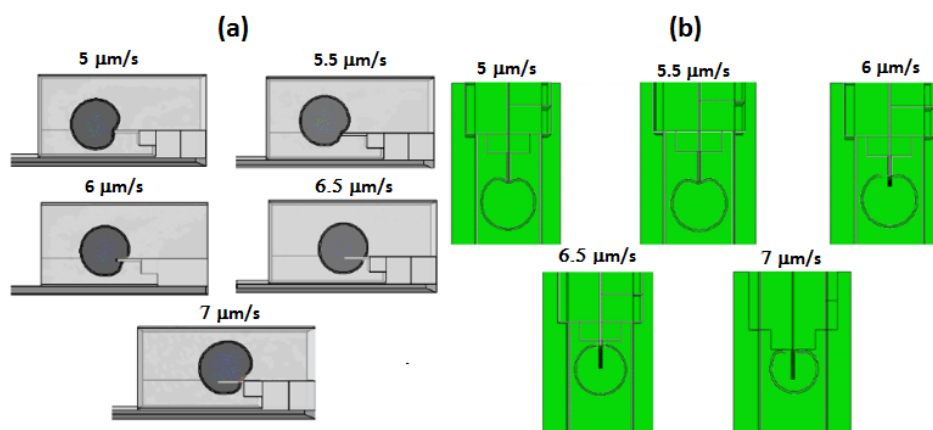


Figure 19. Simulation results of the velocity optimization, (a) side view and (b) top view.

Table 1. Flow rate optimization result.

Velocity ($\mu\text{m/s}$)	Flow Rate (pL/min)	Penetration
5.0	18.9	No
5.5	20.8	No
6.0	22.7	Yes (middle)
6.5	24.6	Yes (full)
7.0	26.5	Yes (excessive)

Finally, the velocity of $6.5 \mu\text{m/s}$ that was optimized in the last section was applied at the inlet. The streamline plot of the water flow in the Y-shaped microchannel at the time of 5 and 35 s are shown in Figure 20. At 35 s, the highest flow was moving toward the long side of the microchannel, which led to migration of cell to nanoneedle side. From the results, the cells flew in a queue towards the long side of the Y-shaped microchannel, which leads to the cells migrating to the nanoneedle. The results show that the single cell can reach to the nanoneedle for penetration. Since the cell wall of the yeast cell is harder than the plasma membrane, the nanoneedle penetration in the cell wall ensures the penetration into plasma membrane.

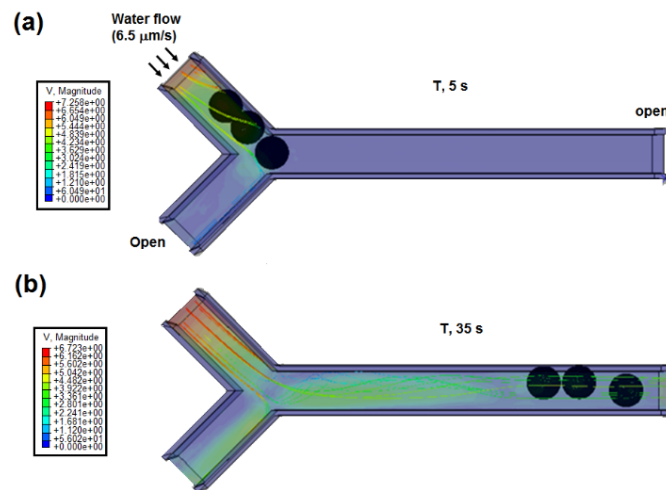


Figure 20. Streamline plot of the water flow in the Y-shaped microchannel after (a) 5 s and (b) 35 s.

The cell extraction process in the microfluidic device was also simulated at different time (Figure 21). It is important to analyze two or more cells by the same microfluidic device. Velocity of $6.5 \mu\text{m/s}$ was used since it showed no effect on the nanoneedle at the inlet, and the other ends were set to open. It was clearly observed that the cells were moved toward the both outlets one after another, which indicated the advantages of two holes to extract the cells fast without clogging of cells.

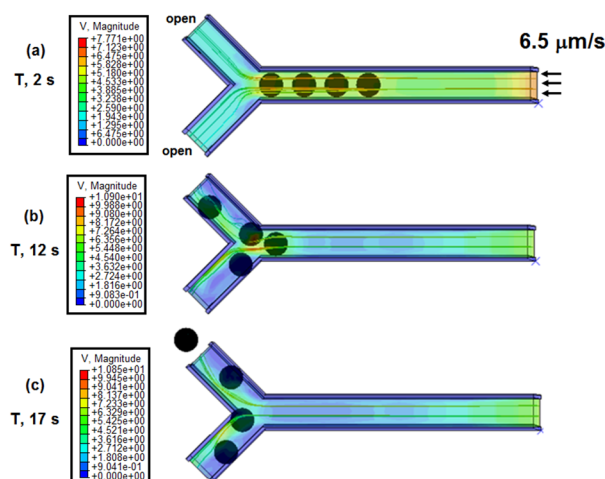


Figure 21. Waste collection simulation results showing the cell direction and the velocity streamlines at (a) 2 s; (b) 12 s; and (c) 17 s.

4. Conclusions

Single cell analysis has become an important field in the medical research and diagnoses. The temperature of a cell in particular is able to reveal vital information on cells' activities, mechanics and development. In this paper, a nanoneedle-microfluidic system to measure single cell temperature was proposed. The design was divided into three main stages, starting with nanoneedle design optimization and mechanical and electrical characterization; then integration with a microfluidic channel; and finally obtaining temperature measurement curve. Tungsten was chosen as the sensing material and the results showed that a rectangular shaped sensor with a gap of 10.8 μm gave an equally distributed current density within the sensor, and a 90 nm^2 cross-sectional area caused minimal damage to the cell. The mechanical characterization study and the nanoneedle showed to be able to resist ramp force applied on it up to 22.5 μN before went into failure. Electrical measurement of the cell showed that the current only moved within the nanoneedle and the nanoneedle was independent of the cell conductivity. The thermal characterization within the cell showed that a current difference of 50 nA could be observed, giving a resolution of 0.02 $^{\circ}\text{C}$ in the range of 24–60 $^{\circ}\text{C}$. The nanoneedle reached equilibrium temperature in 10 ms. A Y microchannel design was optimized to have of 63 μm^2 , considering the effect of the nanoneedle to the flow of water. A flow rate of 24.6 pL/min allowed for cell penetration causing minimal damage to the cell. This system is able to measure the intracellular temperature of single cells and has the potential to be used in biomedical application such as drug delivery.

Acknowledgments: The research was supported by the Ministry of Higher Education of Malaysia (grant No. 4L640 and 4F351), and Universiti Teknologi Malaysia (grant No. 03E11, 03G47, 02G46, 03H82, and 03H80); we thank them for funding this project and for their endless support.

Author Contributions: All authors contributed equally in the presented research work.

Conflicts of Interest: The authors declare no conflict of interest.

References

1. Sang Kyu, K.; Hyunmin, C.; Hye-Jung, P.; Dohyoung, K.; Jeong Min, L.; Bong Hyun, C. Nanogap biosensors for electrical and label-free detection of biomolecular interactions. *Nanotechnology* **2009**, *20*. [[CrossRef](#)]
2. Esfandyarpour, R.; Javanmard, M.; Koochak, Z.; Esfandyarpour, H.; Harris, J.S.; Davis, R.W. Label-free electronic probing of nucleic acids and proteins at the nanoscale using the nanoneedle biosensor. *Biomicrofluidics* **2013**, *7*. [[CrossRef](#)] [[PubMed](#)]
3. Esfandyarpour, R.; Javanmard, M.; Koochak, Z.; Harris, J.S.; Davis, R.W. Nanoelectronic impedance detection of target cells. *Biotechnol. Bioeng.* **2014**, *111*, 1161–1169. [[CrossRef](#)] [[PubMed](#)]
4. Goda, T.; Miyahara, Y. Label-free and reagent-less protein biosensing using aptamer-modified extended-gate field-effect transistors. *Biosens. Bioelectron.* **2013**, *45*, 89–94. [[CrossRef](#)] [[PubMed](#)]
5. Goda, T.; Tabata, M.; Sanjoh, M.; Uchimura, M.; Iwasaki, Y.; Miyahara, Y. Thiolated 2-methacryloyloxyethyl phosphorylcholine for an antifouling biosensor platform. *Chem. Commun.* **2013**, *49*, 8683–8685. [[CrossRef](#)] [[PubMed](#)]
6. Lecault, V.; White, A.K.; Singhal, A.; Hansen, C.L. Microfluidic single cell analysis: From promise to practice. *Curr. Opin. Chem. Biol.* **2012**, *16*, 381–390. [[CrossRef](#)] [[PubMed](#)]
7. Gao, D.; Liu, H.; Jiang, Y.; Lin, J.-M. Recent advances in microfluidics combined with mass spectrometry: Technologies and applications. *Lab Chip* **2013**, *13*, 3309–3322. [[CrossRef](#)] [[PubMed](#)]
8. Zheng, Y.; Nguyen, J.; Wei, Y.; Sun, Y. Recent advances in microfluidic techniques for single-cell biophysical characterization. *Lab Chip* **2013**, *13*, 2464–2483. [[CrossRef](#)] [[PubMed](#)]
9. Evanko, D. Sensors and probes: A thermometer for cells. *Nat. Method* **2012**, *9*, 328. [[CrossRef](#)]
10. McCabe, K.M.; Hernandez, M. Molecular thermometry. *Pediatr. Res.* **2010**, *67*, 469–475. [[CrossRef](#)] [[PubMed](#)]
11. Li, S.; Zhang, K.; Yang, J.-M.; Lin, L.; Yang, H. Single quantum dots as local temperature markers. *Nano Lett.* **2007**, *7*, 3102–3105. [[CrossRef](#)] [[PubMed](#)]
12. Donner, J.S.; Thompson, S.A.; Kreuzer, M.P.; Baffou, G.; Quidant, R. Mapping intracellular temperature using green fluorescent protein. *Nano Lett.* **2012**, *12*, 2107–2111. [[CrossRef](#)] [[PubMed](#)]

13. Binslem, S.A.; Ahmad, M.R.; Awang, Z. Intracellular thermal sensor for single cell analysis-short review. *J. Teknol.* **2015**, *73*, 6.
14. Yang, J.-M.; Yang, H.; Lin, L. Quantum dot nano thermometers reveal heterogeneous local thermogenesis in living cells. *ACS Nano* **2011**, *5*, 5067–5071. [[CrossRef](#)] [[PubMed](#)]
15. Lee, J.; Govorov, A.O.; Kotov, N.A. Nanoparticle assemblies with molecular springs: A nanoscale thermometer. *Angew. Chem. Int. Ed.* **2005**, *44*, 7439–7442. [[CrossRef](#)] [[PubMed](#)]
16. Espenel, C.; Giocondi, M.-C.; Seantier, B.; Dosset, P.; Milhiet, P.-E.; Le Grimellec, C. Temperature-dependent imaging of living cells by afm. *Ultramicroscopy* **2008**, *108*, 1174–1180. [[CrossRef](#)]
17. Gota, C.; Okabe, K.; Funatsu, T.; Harada, Y.; Uchiyama, S. Hydrophilic fluorescent nanogel thermometer for intracellular thermometry. *J. Am. Chem. Soc.* **2009**, *131*, 2766–2767. [[CrossRef](#)]
18. Brites, C.D.S.; Lima, P.P.; Silva, N.J.O.; Millan, A.; Amaral, V.S.; Palacio, F.; Carlos, L.D. Thermometry at the nanoscale. *Nanoscale* **2012**, *4*, 4799–4829. [[CrossRef](#)]
19. Wang, C.; Xu, R.; Tian, W.; Jiang, X.; Cui, Z.; Wang, M.; Sun, H.; Fang, K.; Gu, N. Determining intracellular temperature at single-cell level by a novel thermocouple method. *Cell Res.* **2011**, *21*, 1517–1519. [[CrossRef](#)] [[PubMed](#)]
20. Vyalikh, A.; Wolter, A.U.B.; Hampel, S.; Haase, D.; Ritschel, M.; Leonhardt, A.; Grafe, H.-J.; Taylor, A.; Krämer, K.; Büchner, B.; et al. A carbon-wrapped nanoscaled thermometer for temperature control in biological environments. *Nanomedicine* **2008**, *3*, 321–327. [[CrossRef](#)] [[PubMed](#)]
21. Gao, L.; Wang, L.; Li, C.; Liu, Y.; Ke, H.; Zhang, C.; Wang, L.V. Single-cell photoacoustic thermometry. *J. Biomed. Opt.* **2013**, *18*. [[CrossRef](#)] [[PubMed](#)]
22. Inomata, N.; Toda, M.; Sato, M.; Ishijima, A.; Ono, T. Pico calorimeter for detection of heat produced in an individual brown fat cell. *Appl. Phys. Lett.* **2012**, *100*. [[CrossRef](#)]
23. Ahmad, M.R.; Nakajima, M.; Kojima, M.; Kojima, S.; Homma, M.; Fukuda, T. Instantaneous and quantitative single cells viability determination using dual nanoprobe inside esem. *IEEE Trans. Nanotechnol.* **2012**, *11*, 298–306. [[CrossRef](#)]
24. ElShimy, H.; Nakajima, M.; Arai, F.; Fukuda, T. *Sensing Temperature in Water Using fib cvd Nano Thermal Sensors*, Proceedings of the 2007 International Symposium on Micro-NanoMechatronics and Human Science, (MHS'07), Nagoya, Japan, 11–14 November 2007; pp. 7–11.
25. ElShimy, H.; Nakajima, M.; Imaizumi, Y.; Arai, F.; Fukuda, T. Fabrication of fib-cvd nanotemperature sensor probe for local temperature sensing in water environments. *J. Robot. Mechatron.* **2007**, *19*, 512–518.
26. Tritt, T.M. *Thermal Conductivity, Theory, Properties, and Applications*; Springer: New York, NY, USA; Boston, MA, USA; Dordrecht, The Netherlands; London, UK; Moscow, Russia, 2004.



© 2016 by the authors; licensee MDPI, Basel, Switzerland. This article is an open access article distributed under the terms and conditions of the Creative Commons Attribution (CC-BY) license (<http://creativecommons.org/licenses/by/4.0/>).